ACS NANO

www.acsnano.org

ARTICLE

Imaging Negative Charge around Single Vanadium Dopant Atoms in Monolayer Tungsten Diselenide Using 4D Scanning Transmission Electron Microscopy

Djordje Dosenovic, Samuel Dechamps, Kshipra Sharma, Jean-Luc Rouviere, Yiran Lu, Martien Ilse den Hertog, Luigi Genovese, Simon Mutien-Marie Dubois, Jean-Christophe Charlier, Matthieu Jamet, Alain Marty, and Hanako Okuno*

Cite This: *ACS Nano* 2024, 18, 23354–23364

Read Online

ACCESS | Metrics & More | Article Recommendations | Supporting Information

ABSTRACT: **There has been extensive activity exploring the doping of semiconducting two-dimensional (2D) transition metal dichalcogenides in order to tune their electronic and magnetic properties. The outcome of doping depends on various factors, including the intrinsic properties of the host material, the nature of the dopants used, their spatial distribution, as well as their interactions with other types of defects. A thorough atomic-level analysis is essential to fully understand these mechanisms. In this work, the vanadium-doped WSe_2 monolayer grown by molecular beam epitaxy is investigated using four-dimensional scanning transmission electron microscopy (4D-STEM). Through center-of-mass-based reconstruction, atomic-scale maps are produced, allowing the visualization of both the electric field and the electrostatic potential around individual V atoms. To provide quantitative insights, these results are successfully compared to multislice image simulations based on ab initio calculations, accounting for lens aberrations. Finally, a negative charge around the V dopants is detected as a drop in the electrostatic potential, unambiguously demonstrating that 4D-STEM can be used to detect and to accurately analyze single-dopant charge states in semiconducting 2D materials.**

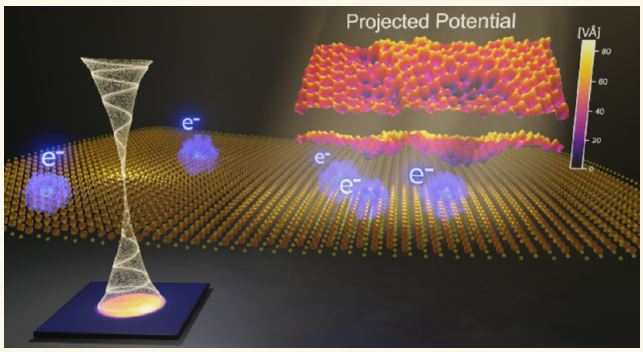

KEYWORDS: *4D-STEM, electrostatic potential mapping, electron ptychography, WSe_2, single-dopant atom, charge state, 2D materials*

Downloaded via UNIV CATHOLIQUE DE LOUVAIN on August 28, 2024 at 13:42:00 (UTC).
See https://pubs.acs.org/sharingguidelines for options on how to legitimately share published articles.

Owing to their versatile electronic properties and reduced dimensionality, layered two-dimensional (2D) materials have emerged as promising candidates for exceptionally compact devices.[1] Among these materials, transition metal dichalcogenides (TMDs) have received special attention due to their often semiconducting nature and the ability to fine-tune their electronic structure, making them ideal for innovative logic and memory devices.[2−4] In recent years, significant progress has been made in the synthesis of 2D materials, enabling the creation of materials tailored to specific properties.[5] However, the properties of these synthesized materials are significantly influenced by intrinsic and extrinsic structural imperfections such as vacancies, grain boundaries, and dopants. The resulting functionality of the corresponding 2D material is intricately linked to the electronic properties of these defects as well as their concentration and distribution within the sample. Molecular beam epitaxy (MBE) has emerged as a valuable process for enhancing the complexity of scalable engineered 2D materials. Notably, it enables precise control over the introduction of dopant atoms into 2D layers, thus offering a means to finely adjust the material properties.[6,7] In the context of otherwise nonmagnetic TMDs, doping with magnetic elements like V, Mn, Fe, and Co in low concentrations has the potential to induce long-range ferromagnetic ordering. This leads to the

Received: May 17, 2024
Revised: July 29, 2024
Accepted: August 1, 2024
Published: August 15, 2024

© 2024 American Chemical Society

https://doi.org/10.1021/acsnano.4c06561
ACS Nano 2024, 18, 23354−23364

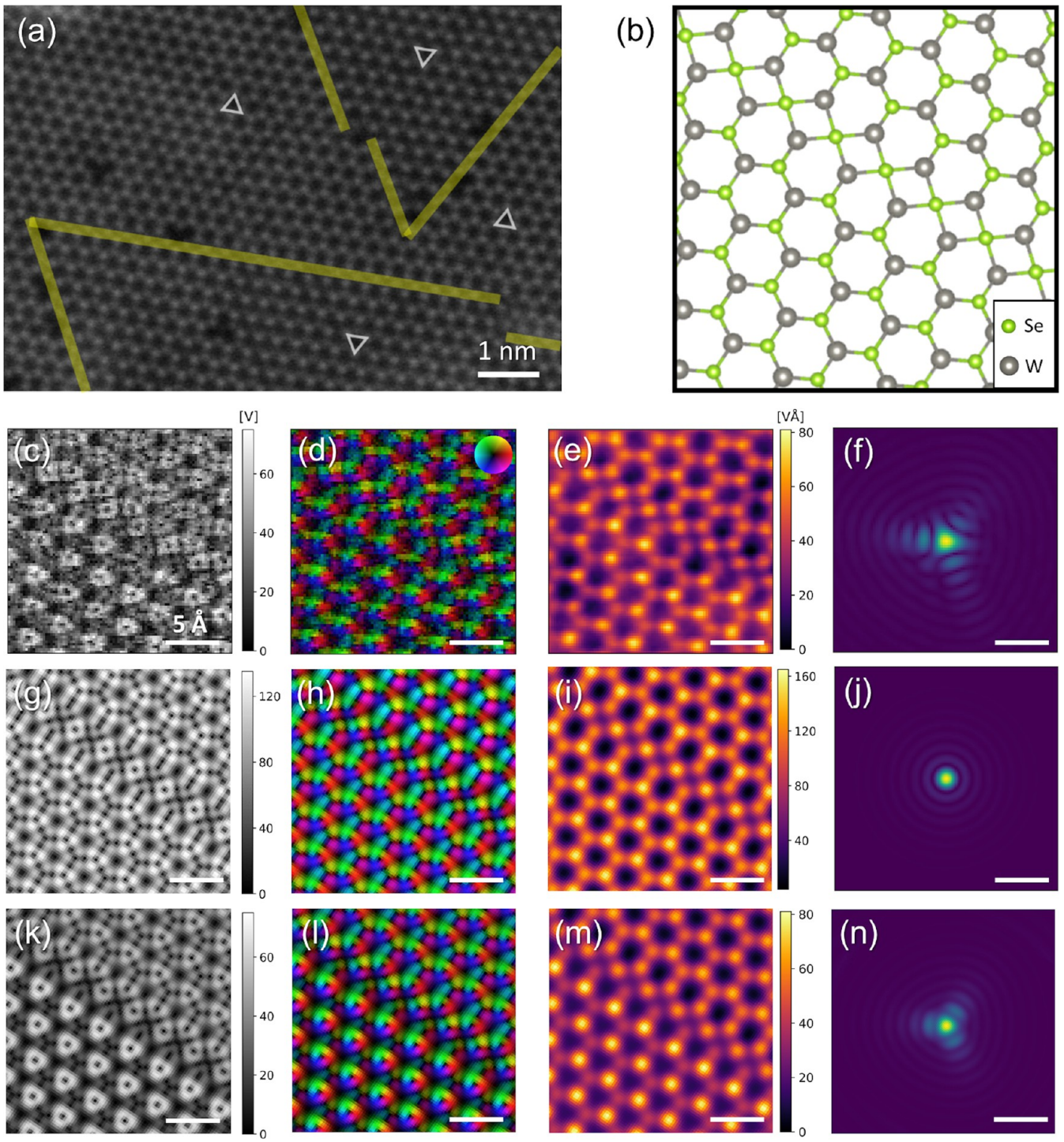

Figure 1. (a) HAADF image of the V-doped WSe_2 sample. MTBs are indicated by yellow lines. (b) DFT-relaxed model of MTB in WSe_2 used for the image simulations. (c, d) Experimental map of projected electric field around a MTB reconstructed by the CoM method and (e) the corresponding projected potential map. (f) Ptychographic reconstruction of the electron probe used during the acquisition of the 4D data set. (g, h) Projected electric field map reconstructed from a simulated 4D data set without any lens aberrations and (i) the corresponding projected potential map. (j) Simulated aberration-free electron probe. (k, l) Projected electric field map and (m) potential map reconstructed from simulated 4D data set with defocus = −9 nm and A2 = 220 nm. (n) Simulated aberrated electron probe. All of the scale bars in panels (c−n) correspond to 5 Å.

creation of what are known as diluted 2D magnetic semiconductors, where the ferromagnetic ordering can be controlled by a gate voltage.[8−10] The theoretical predictions of long-range ferromagnetic ordering in such systems[11] have been experimentally confirmed.[12] However, it is worth noting that the magnetic moment induced by dopant atoms is expected to be suppressed when the dopants carry a negative charge due to the occupation of defect-induced states.[13,14] Therefore, the ability to investigate the atomic-scale structure, the local chemical environment, and the charge state of the dopant is crucial for a comprehensive understanding of the properties of the 2D materials. While local probe techniques, namely, scanning

https://doi.org/10.1021/acsnano.4c06561
ACS Nano 2024, 18, 23354−23364

tunneling microscopy/spectroscopy (STM/STS), are commonly used for the analysis of local electronic structure, the information coming from electronic and atomic structures is difficult to dissociate. The chemical identification of impurities and other defects using such methods is often challenging and ambiguous.[15] In this context, aberration-corrected scanning transmission electron microscopy (AC-STEM) equipped with analytical spectroscopy techniques such as electron energy loss spectroscopy (EELS) stands out as the most effective tool for structural and chemical analysis at the atomic scale.

Today, with the development of the differential phase contrast (DPC) imaging technique, additional information going beyond the identification of chemical species and their positions can be accessed. The DPC technique measures the deviation of the electron beam off the optical axis induced by the in-plane components of local electric and magnetic fields.[16] This technique was first demonstrated using a segmented detector, allowing for an approximate estimation of the electron beam deflection. Recent developments in pixelated electron detectors enable increased measurement capabilities. In the so-called four-dimensional scanning transmission electron microscopy (4D-STEM) acquisition mode,[17] a 2D diffraction pattern is collected for each beam position allowing a more precise measurement of the beam deflection. The deviation of the center of mass (CoM) of the transmitted electron beam in each collected diffraction pattern can be directly related to the local electric field.[18,19] The CoM approach is therefore rather straightforward, contrary to other phase retrieval techniques such as ptychography that requires more sophisticated computational processing.[20] By solving the Poisson's equation, other associated fundamental quantities such as the electrostatic potential and charge density can be obtained from the electric field.[19] Nevertheless, the DPC technique is not yet used in the characterization of 2D materials on a routine basis. Previous demonstrations have been limited to model systems, i.e., pristine and point defect structures in exfoliated MoS_2[21] and line defects in MoS_2 and WS_2 created by electron irradiation inside the microscope.[22,23] The imaging of the electric field of single Si dopants in monolayer graphene grown by chemical vapor deposition (CVD) has also been used to distinguish between two different dopant coordination states.[24] The widespread application of the method in studying real synthesized materials is hindered by experimental difficulties related to long acquisition times, sample stability under the beam, and transfer-related polymer contamination, as well as challenges in quantitative interpretation of the reconstructed electric field, potential, and charge density images. Importantly, the influence of residual lens aberrations on the electric field images reconstructed by DPC-CoM has often been mentioned but rarely discussed in detail.[22,24,25] Recently, DPC-CoM has been studied to resolve the electron charge density of individual atomic columns or single atoms in 2D materials to access fundamental material information such as the valence electron distribution. However, an important current limitation of the technique regarding the influence of the probe size has been pointed out.[26,27]

In this work, we demonstrate that defect-induced charge redistribution can be indirectly inferred from electrostatic potential maps reconstructed using 4D-STEM CoM, showing long-range perturbation of the background potential around dopant species, contrary to the commonly used approach of charge density measurement. We start by establishing a workflow for quantitatively analyzing 4D data sets. This is achieved by incorporating density functional theory (DFT)-based STEM multislice simulations, which take into account the residual aberrations inherent in the experimental data. To estimate these residual aberrations, we conduct a ptychographic probe reconstruction for each of the experimental 4D data sets. We apply this methodology to achieve atomic resolution mapping of the electric field within a V-doped WSe_2 monolayer grown directly on graphene/Pt using molecular beam epitaxy (MBE). Finally, the local electric field and the potential around single atom V dopants are measured using 4D-STEM CoM reconstruction, where a potential drop induced by the negatively charged dopant atoms is detected, in analogy to previous STM observations on a similar system.[28]

RESULTS AND DISCUSSION

The V-doped WSe_2 was grown by MBE on the CVD graphene monolayer as grown on Pt/Si substrate, using the same growth process shown in a previous work to synthesize the V-doped WSe_2 on graphene/SiC for the STM study.[28] The WSe_2/graphene heterostack was transferred by polymer-assisted wet transfer using the electrochemical method,[29] followed by surface cleaning. The STEM imaging, EELS spectrum imaging, and 4D-STEM acquisition are performed in low-voltage (80 kV) condition to minimize the creation of chalcogen vacancies in TMDs.[30] Experimental 4D-diffraction data sets for the CoM analysis are registered using a fast pixelated camera. Simulated diffraction patterns are obtained using STEM multislice simulations, where the electrostatic potential of the (V-doped) WSe_2 monolayer estimated by DFT is used to model the specimen. The electron beam is simulated taking into account microscope conditions such as acceleration voltage, convergence angle, and lens aberration coefficients. The center of mass of the transmitted electron beam is measured from both the experimental and simulated diffraction patterns and subsequently converted into the projected electric field using Ehrenfest theorem.[18,19] Finally, the experimental and simulated images of projected electrostatic potential are generated by integration in Fourier space.[31] Figure 1a shows the high angle annular dark field (HAADF) image of V-doped WSe_2 on graphene that exhibits relatively clean and highly crystalline structures, where two typical structural anomalies are found; individual point defects at the W sites and triangular inversion domains (TIDs). The HAADF image confirmed the presence of a light atom replacing W atom at each point defect (Figure S1), suggesting successful vanadium doping as demonstrated elsewhere.[28,32] TIDs are rarely observed in pristine WSe_2 due to their high formation energy.[33] In our sample, TID networks with different densities are observed depending on the local dopant concentration (Figure S2). The addition of vanadium to the growth system has been demonstrated to lower the formation energy[34] and promote the appearance of TIDs consisting of stable 4|4P line defects, so-called mirror twin boundaries (MTBs) under the Se deficient condition, which is often unavoidable in MBE growth.[35] Figure 1b illustrates the atomistic model of MTBs observed in V-doped WSe_2, as relaxed by DFT structural optimization. Figure 1c−e shows 2D images of the projected electric field and the electrostatic potential around a MTB reconstructed by the CoM method. Given the symmetry of the 4|4P domain junction, it is expected that the electric field and the electrostatic potential of WSe_2 will exhibit identical contrast patterns on the two sides of the MTB with 60° rotated mirror crystal symmetry. However, the reconstructed images of the projected electric field and potential present substantially different contrast. Since the grain boundary structure is known

https://doi.org/10.1021/acsnano.4c06561
ACS Nano 2024, 18, 23354−23364

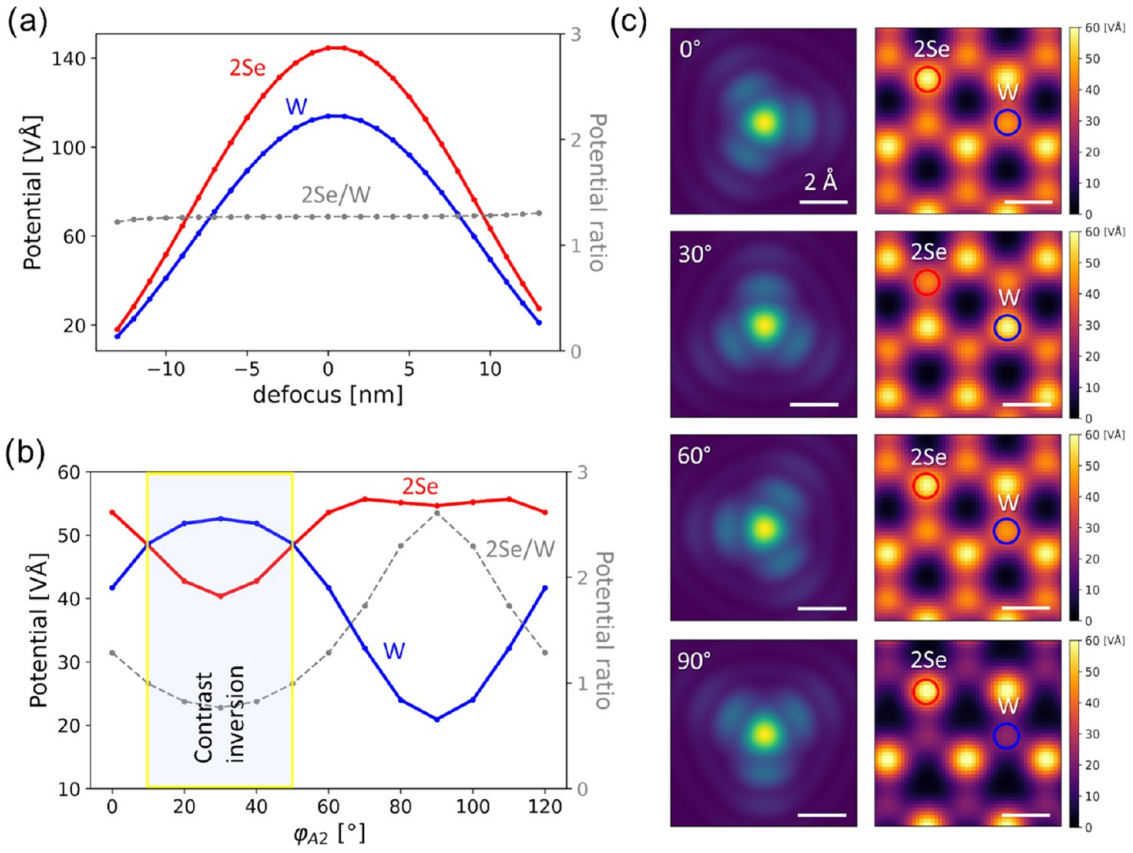

Figure 2. (a) Average projected potential around 2Se (red) and W (blue) atomic columns and potential ratio (dashed gray) from a series of multislice simulations with different values of defocus and without any additional aberrations. The reference zero defocus is defined on the W plane, and the positive focus is defined as underfocus. (b) Average projected potential around atomic columns and potential ratio from a series of multislice simulations with the fixed value of defocus (def = −9 nm) and the magnitude of 3-fold astigmatism (A2 = 220 nm) and the varying azimuthal angle of A2 aberration. (c) Typical examples of simulated probe and the reconstructed projected potential for the characteristic values of A2 azimuthal angles: φ_{A2} = 0, 30, 60, 90°. All of the scale bars in the probe and potential images correspond to 2 Å.

from the HAADF imaging and the energy stability arguments,[33] the positions of W and 2Se in the reconstructed images are unambiguously determined (Figure S3). The intensities of W atoms in the upper right corner in Figure 1e are higher than the intensities of neighboring 2Se columns, while the intensity ratio of these two columns is inversed on the opposite side of a MTB. This variation in intensity as a function of crystal orientation has often been studied in atomic resolution HAADF images, as a consequence of residual aberrations.[26,36,37] Figure 1g−i depicts the projected electric field and the electrostatic potential reconstructed from the DFT-based STEM multislice simulation, including the main microscopy parameters but in the aberration-free condition (Figure 1j).

Indeed, without probe aberrations, the reconstructed projected electric field and potential exhibit a mirror symmetry around the MTB as expected. In order to survey the residual aberration present in the probe, we perform the ptychographic probe reconstruction directly from the experimental 4D data set used to obtain the electric field and potential shown in Figure 1c−e. The reconstructed probe intensity (Figure 1f) exhibits a triangular shape commonly attributed to the effect of residual 3-fold aberrations (i.e., A2 and D4).[36,38,39] The corresponding probe deconvolved object phase reconstructed by ptychography is shown in Figure S7. Furthermore, the overall magnitudes of electric field and potential predicted by the aberration-free simulation exceed the experimental values by about a factor of 2, even after taking into account the spatial incoherence of the probe, as previously observed.[22,24] This attenuation in intensity is assumed to be due to defocus and other spherical aberrations that contribute to the beam broadening.[25]

Figure 2a shows simulations of the atomic column intensity dependence on defocus. The defocus indeed attenuates the intensities of both the W and 2Se atomic columns while their intensity ratio remains constant. The effect of 3-fold aberrations depends on their magnitude as well as on the azimuthal angle φ, which can be understood as the orientation of the triangular probe. A series of multislice simulations are performed with different orientations of A2 astigmatism while the orientation of the crystal is kept constant (Figure 2b,c). The azimuthal angle of the aberration is varied from 0 to 120° with an increment of 10°, and the average potential around the 2Se and W atomic columns is evaluated for each simulated reconstructed projected potential. The intensities of the 2Se and W columns shown in Figure 2b,c are strongly dependent on the azimuthal angle φ_{A2}. In a certain range of orientations ($10° < \varphi_{A2} < 50°$), the W atoms appear brighter than the 2Se atomic columns, leading to the contrast inversion, whereas HAADF imaging under the same beam conditions is found to be more resistant to the effect of A2 astigmatism (Figure S4).

In practice, the orientation of the electron probe is quite stable during an experiment. However, the 2D layers are often polycrystalline, and the orientation of the crystal with respect to the electron probe can be arbitrary. For this reason, the contrast will strongly depend on the local orientation of the

https://doi.org/10.1021/acsnano.4c06561
ACS Nano 2024, 18, 23354−23364

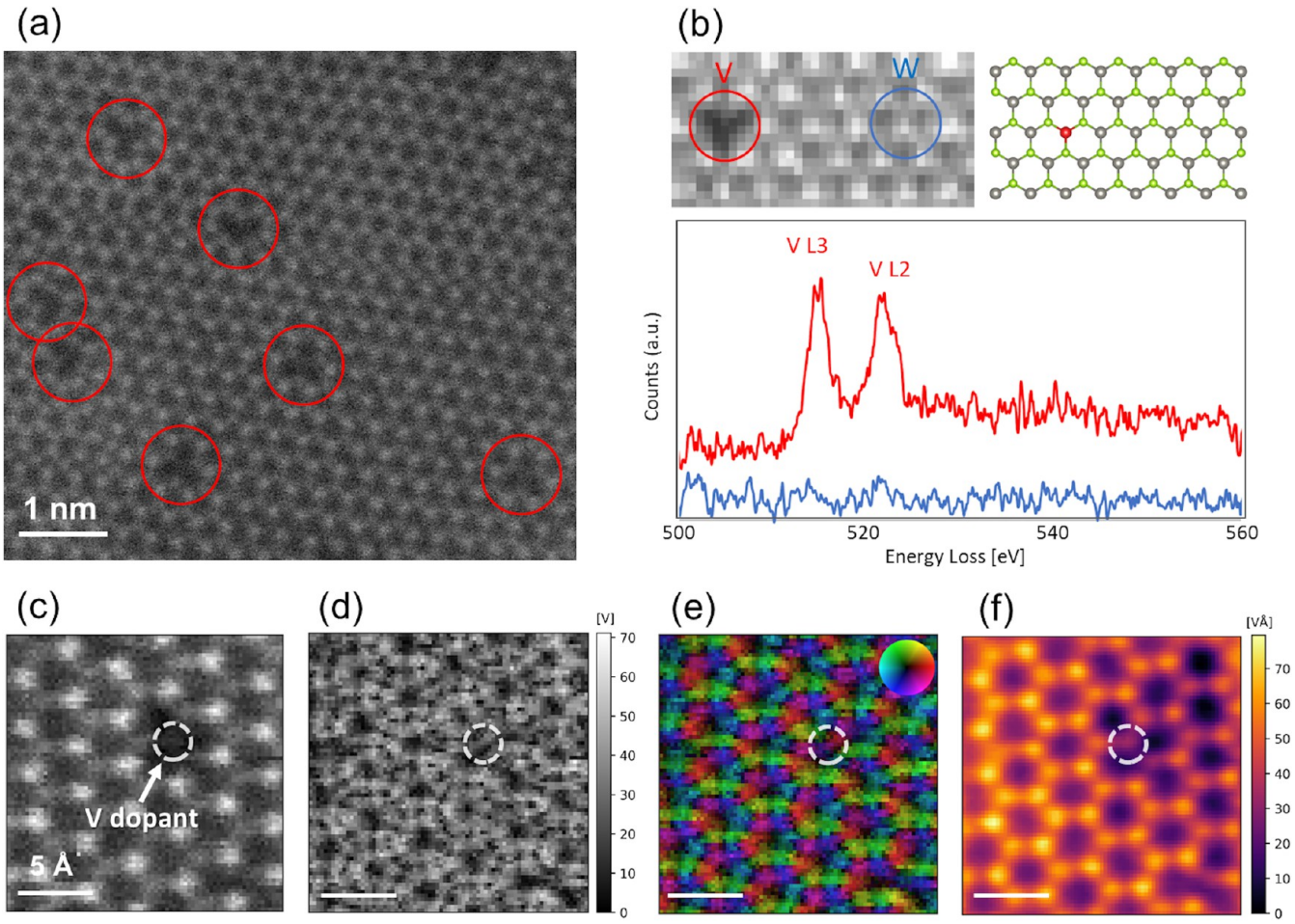

Figure 3. (a) HAADF image showing the distribution of point defects (red circles) in V-doped WSe_2. (b) EELS spectrum around a point defect at the tungsten site (red) indicating incorporation of vanadium dopant and the reference spectrum around the tungsten atom (blue). (c) Virtual ADF image reconstructed from a 4D data set acquired around vanadium dopant. (d) Magnitude of projected electric field, (e) its vector whose direction is given by the color wheel, and (f) the corresponding projected electrostatic potential reconstructed from the 4D data set.

crystal in the region of interest. As already shown in Figure 1, an acquisition around a 4|4P MTB results in a significantly different contrast at the two sides of the domain boundary since the two crystallites are misoriented by 60° and the reconstructed projected potential on the two sides of the MTB would correspond roughly to the potential reconstructed from the simulations with $\varphi_{A2} = 30°$ and $\varphi_{A2} = 90°$, shown in Figure 2c.

In order to include the experimentally used microscope parameters in the simulations, the angle of the apparent 3-fold aberration is measured directly from the reconstructed probe image shown in Figure 1f. The virtual defocus and magnitude of A2 are then fine-tuned by comparing the simulated intensities of the W and 2Se columns with those obtained experimentally in defect-free reference regions. Figure 1k–m shows the images of the projected electric field and electrostatic potential, respectively, reconstructed from the simulation taking into account these two parameters (defocus = −9 nm and A2 = 220 nm), giving the electron probe intensity shown in Figure 1n. The overall intensities are now in agreement with the experiment by taking into account defocus effects, while the contrast inversion between the W and 2Se atomic columns on the two sides of the MTB is achieved by setting the corresponding A2 astigmatism. Here, it should be noted that the 3-fold aberration is considered only with A2 astigmatism as a single parameter. The obtained value (A2 = 220 nm) might include other higher-order aberrations such as D4, which may explain the value being much higher than A2 usually measured in the microscope. Similarly, the fixed defocus might include other spherically symmetric aberrations (focal spread and third-order (C3) and fifth-order (C5) spherical aberrations). The combined effect of all aberrations is thus approximated by fitting only two virtual coefficients (defocus and A2). This approach significantly reduces the number of variables in the simulations without a major loss on the quantitative comparison and allows acquiring a reliable simulation for each experimental data set.

This quantitative analytical process is applied to study the local potential state induced by single V-dopant atoms incorporated into the WSe_2 monolayer deposited on the graphene monolayer. Figure 3a shows the HAADF image of the V-doped WSe_2 layer, where a large concentration of point defects at W sites is observed both in pristine regions and in mirror domain boundaries. Additional local chemical analysis by EELS spectroscopy unambiguously confirms the presence of V single atom dopants substituting for W atoms (Figure 3b). A 4D-STEM acquisition is then performed around a single V atom, from which we reconstruct the real space images of the projected electric field and projected potential (Figure 3d–f). The V-dopant exhibits higher visibility in the reconstructed electric field and electrostatic potential maps than in the HAADF image (Figure 3a) and the ADF image virtually reconstructed from the

https://doi.org/10.1021/acsnano.4c06561
ACS Nano 2024, 18, 23354–23364

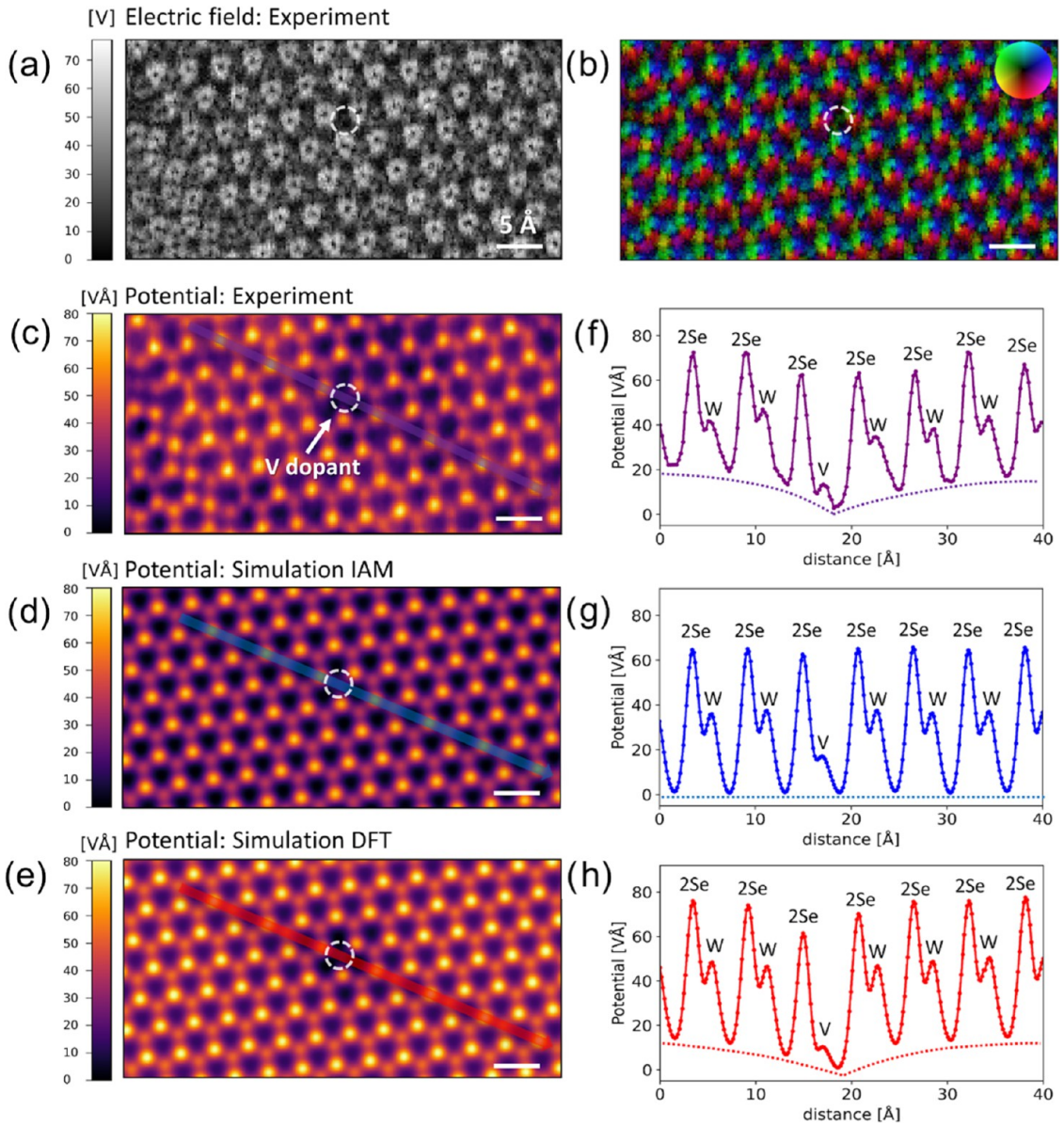

Figure 4. (a, b) Experimentally measured magnitude and direction of the projected electric field. (c) Experimental image of the projected electrostatic potential around a V-dopant atom. (d, e) Images of the projected potential reconstructed from multislice simulation with def = −9 nm, A2 = 120 nm where the input potential of V-doped WSe_2 is generated from IAM (neutral V-dopant) and DFT (charged V-dopant), respectively. (f−h) Line profiles through the regions indicated in the potential images (c−e), respectively. The dashed lines point out the variation of the background potential around a V-dopant atom.

same data set (Figure 3c). The use of DPC-CoM for the simultaneous visualization of light and heavy elements has already been demonstrated and discussed.[40] According to our results presented in Figure 2, the intensity ratio 2Se/W as well as the visibility of light elements in the potential map varies as a function of the residual 3-fold astigmatism and defocus. Here, the potential map is affected by the residual 3-fold astigmatism effect, and the W site gives more intensity than the 2Se site, which is confirmed by the atomic positions attributed in the corresponding virtual ADF image.

A peculiar potential drop around the V-dopant atom is detected in the reconstructed potential image in Figure 3f. To elucidate this phenomenon, the electronic structure of the defective monolayer is computed using DFT (see Section 10 in the Supporting Information). In line with previous works, substitutional V atoms are shown to induce p-type doping by introducing states close to the valence band maximum, whose net negative charge has been measured by local probe techniques.[28,32,41] The observed potential drop is supposed to be a consequence of this charge state. To investigate this assumption, an experimentally obtained projected electrostatic potential map (Figure 4c) is compared with those reconstructed from two simulated data sets (Figure 4d,e). While the first multislice simulation estimates the potential using the independent atom model (IAM), with a neutral dopant, the second model is based on density functional theory (DFT), where a net negative charge is assigned to vanadium.

Our 4D-STEM measurement gives access to three projected physical quantities, namely, the electric field, the potential, and the charge density. Among the three, we focus on the electrostatic potential for comparison with the DFT-based simulations. Stemming from its vectorial nature, the 2D image

https://doi.org/10.1021/acsnano.4c06561
ACS Nano 2024, 18, 23354−23364

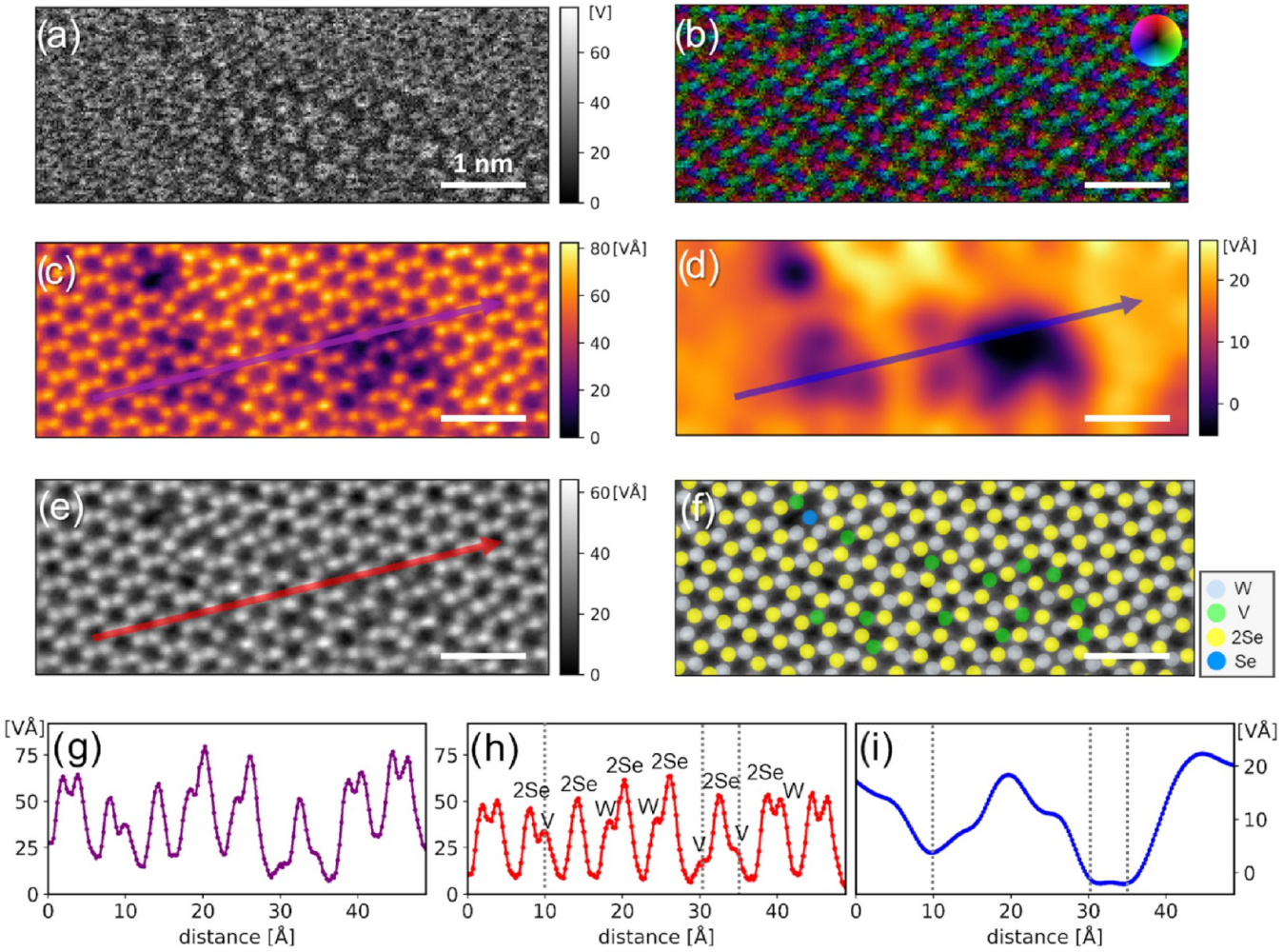

Figure 5. (a) Magnitude of projected electric field. (b) Direction of the projected electric field. (c) Projected potential derived from the electric field shown in panels (a, b). (d) Background potential obtained by Gaussian filtering of the image (c). (e, f) Background subtracted potential image with atomic species identification. (g−i) Line profiles along the arrows indicated in panels (c−e), respectively.

representation of the electric field as measured directly by the CoM method is not straightforward (Figure 4a,b). On the contrary, both the electrostatic potential and the charge density are scalar fields obtained by integration and divergence of the electric field, respectively, which can be easily represented in a real-valued 2D image. Additionally, charge effects appear more distinctly in the potential map than in the corresponding charge density map (Figure S5). Finally, integration has a smoothing effect that reduces numerical noise, while divergence has the opposite effect. All of these arguments go in favor of using the images of the reconstructed projected potential for the analysis of the dopant charge states. We first identify the values of defocus and A2 astigmatism from the data set used in Figure 4, which reproduce the experimental conditions, as explained above. In contrast to the data set shown in Figure 3, the analyzed area exhibits a different aberration effect, where the intensity of the W columns is lower than that of the 2Se columns. Subsequently, we compare the reconstructed potential image computed from IAM and DFT with the experimental parameters including the aberrations estimated from the experimental data. While the former simulation predicts the intensities of the individual W, 2Se, and V atoms with satisfactory accuracy (Figure 4g), it fails to reproduce the experimentally observed background intensity variation around the V atom (Figure 4f). On the other hand, localizing a negative charge of $q = -0.45e$ on the V-dopant in the DFT-based 4D-STEM multislice simulation results in a reconstructed potential that exhibits the background intensity gradient as observed in the experimental data (Figure 4h).

Therefore, we attribute the experimentally observed potential drop to the presence of a negative charge around the V-dopant atom. The presence of the potential drop was additionally confirmed by the ptychography-based object phase reconstruction from the same data set (Figure S8).

Similar doping effects have been detected by STM in WSe_2/graphene/SiC systems,[28,32,41] where the excess charge is taken from the heavily doped graphene on SiC.[28] Since the observed WSe_2/graphene stack is a freestanding heterostructure that was transferred from its growth substrate, it is not clear whether such doping would persist after wet transfer from the native substrate. On top of the above considerations, it is worth noting that the charge state of V-dopant atoms could potentially be affected by electron beam illumination through diverse mechanisms[42] although the precise extent of its influence remains uncertain. Although most of the single V-dopant atoms in our sample exhibit a potential drop, some V atoms are found not to induce this effect. For instance, no potential drop is reported in the vicinity of an impurity at a W site, whose intensity in the

https://doi.org/10.1021/acsnano.4c06561
ACS Nano 2024, 18, 23354−23364

potential image corresponds to a V atom (see Figure S6). In consequence, this point defect is identified as a neutral V-dopant. Since the V dopants in WSe_2 monolayer act as shallow acceptors with transition level of around 0.10 eV, thermal fluctuations or slight local variations in electrostatic environment could explain the simultaneous observations of neutral and charged dopant species.

Regardless of the origin of the negative charge, its detectability is benchmarked on a model system composed of one relatively isolated dopant atom (Figure 4). The synthesized materials, however, contain numerous structural defects and give rise to complex charge interactions.[43,44] To elucidate the sensitivity of V dopants on their neighboring environment, the interactions with surrounding Se vacancies and MTBs, i.e., the most commonly observed defects in our samples, are investigated using DFT (see Section 11 in the Supporting Information). In a nutshell, Se vacancies break the symmetry of the charge distribution, while charge transfer occurs between the MTBs metallic states and the dopant state. In order to investigate the electrostatic potential landscape resulting from complex charge interactions, we perform a 4D-STEM acquisition on a defect-rich area of the sample where numerous dopants can be found in a close vicinity of other point and line defects.

Figure 5a,b shows the electric field of a V-doped WSe_2 layer containing Se vacancies and an MTB network. The calculated projected electrostatic potential shown in Figure 5c exhibits a significant background variation around the observed point defects. In line with the above demonstration of potential drop due to negative charge (Figure 4), we separate the total projected potential (Figure 5c) in two components: (i) the background signal, shown in Figure 5d, obtained by Gaussian filtering of the image of the total potential and (ii) the background subtracted potential map, shown in Figure 5e. A successful background estimation is confirmed with the line profiles shown in Figure 5g–i. The background subtracted image reflects the individual atomic potentials independent of charge states and can be used for the identification of dopant positions and determination of structural arrangements. The attribution of atomic species based on the background subtracted image and taking into consideration the above discussion about 3-fold astigmatism is given in Figure 5f. A total of 14 vanadium dopant atoms are identified in the (2.3×6) nm^2 area of the image, predominantly incorporated in the inversion domain boundaries as previously suggested by DFT calculations.[34] The images of the total potential and background signal (Figure 5c,d) confirm the formation of potential wells of different forms arising around the identified vanadium substitutes. Such a strong background variation cannot be explained by the independent atom model simulations performed on a system with a similar spatial configuration of point defects (Figure S9). Therefore, the potential drop is seen as a consequence of charge-related phenomena, where the shape and the depth of the potential drops are directly related to the distribution of the confined charge.

The CoM-based analytical process outlined in this work can be applied to explore doping effects within more realistic environments, where a precise charge quantification can be achieved by combining large-scale DFT calculations with DFT-based multislice image simulations.

CONCLUSIONS

To summarize, this work delves into a quantitative analytical process based on the CoM method using 4D-STEM and applies it to map the electrostatic potential around vanadium dopants incorporated in WSe_2. We have identified a significant impact of residual spherically symmetric aberrations and 3-fold aberrations under standard acquisition conditions. These aberrations can lead to misinterpretation of the CoM-reconstructed images. Consequently, this highlights the importance of comparing experimental results to simulations that consider the dominant residual aberration terms and other microscope parameters. Indeed, when the experimentally obtained CoM reconstructions are compared to those generated from DFT-based multislice simulations, mimicking the experimental beam conditions, quantitative agreement is found. The electrostatic potential mapping around individual dopant atoms reveals a distinct potential drop associated with certain dopant species. This potential drop is successfully reproduced in DFT-based simulations, indicating the localization of a net negative charge at the V-dopant atom, thereby demonstrating single charge detection sensitivity by using the 4D-STEM CoM method. This finding demonstrates the application of the CoM technique in screening defect charge states and studying charge-related phenomena. Furthermore, the insights gained from this research provide valuable input for theoretical calculations and future studies aimed at elucidating why the material exhibits the observed charge state and what implications it holds for the resulting material properties and magnetic ordering.

METHODS

Sample Growth. The film was grown by molecular beam epitaxy under ultrahigh vacuum (UHV) in a reactor with a base pressure of 5×10^{-10} mbar. Prior to the growth, the Gr/Pt substrate was annealed under UHV at 800 °C during 30 min. The substrate temperature was kept at 340 °C during the film growth, and W and V were coevaporated using electron guns at 0.025 and 0.0025 Å/s deposition rates, respectively, as monitored by quartz balances. Se was evaporated from a Knudsen cell at a pressure of 1×10^{-6} mbar measured at the sample position thanks to a retractable flux gauge. We deposited the equivalent of 0.9 ML of WSe_2 and 0.2 ML of VSe_2 corresponding to a V concentration of 10%. After the growth, the sample was annealed at 800 °C for 15 min under Se flux and then allowed to cool to room temperature. Finally, a 10 nm-thick amorphous selenium layer was deposited.

Scanning Transmission Electron Microscopy. Prior to the observation in the microscope, the as-grown sample is spin coated with a polystyrene layer at 3000 rpm. The coated stack of WSe_2/graphene is then detached from the native Pt substrate by the electrochemical wet transfer method. The floating sample is fished on a TEM grid (C-flat) with 2 μm holes, and the polystyrene layer is dissolved in toluene. The sample is further rinsed in acetone and isopropyl alcohol and left to dry at room temperature. Subsequently, the Se cap is removed by sublimation during heating in vacuum at 250 °C for 1h using a Gatan heating station and holder. The sublimation of the Se cap additionally contributes to the removal of polymer residues from the sample surface. The sample is observed using aberration-corrected FEI Titan Ultimate operating at 80 kV to minimize the beam-induced knock-on damage. A convergence semiangle of 20 mrad was used for all the STEM imaging. The acquisition of HAADF images is done using a beam current of 30 pA and dwell time of 2 μs, while the detector captures electrons scattered above 55 mrad. For EELS analysis, we used a GIF Quantum spectrometer (Gatan) operating at 80 kV. The EELS collection semiangle is 50 mrad. Typical electron beam current is 30 pA. The exposure time is 0.1 s/pixel. The 4D-STEM data are acquired using dwell times in the range of 0.4–0.8 ms and beam currents in the range of 3–16 pA. The diffraction patterns are collected using Medipix3-based Merlin camera (256 × 256 pixels) in continuous 6-bit or 12-bit single-pixel mode at a t_0 threshold of 30 keV.

Data Treatment and 4D-STEM Simulations. The center of mass of each diffraction pattern in the acquired 4D data set is determined

https://doi.org/10.1021/acsnano.4c06561
ACS Nano 2024, 18, 23354–23364

using py4dstem[31] open-source python package, and the projected electric field is calculated as detailed in ref19. The projected potential is then calculated by the integration in Fourier space, and the zero padding factor of 4 was used to ensure the periodic boundary conditions and to prevent edge artifacts. The background estimation was performed by Gaussian filtering (σ = 1.6 Å) of the image of the total potential.

The multislice simulations are performed using abTEM simulation package.[45] The electrostatic potential that serves as input in the simulations is obtained by GPAW[46] as explained below. The independent atom model input potential is obtained using Lobato parametrization.[47] The electron beam in the simulations is defined by setting the acceleration voltage of 80 kV and the semiconvergence angle of 20 mrad corresponding to the conditions used for the experimental acquisitions. Additionally, the probe aberrations are added, namely, defocus and 3-fold astigmatism. The input potential for the multislice simulations is cut into slices with a thickness d_z = 0.2 Å. The simulated 4D data set is then treated in the same way as the experimental data sets as previously explained, and the obtained reconstructed maps are convolved with a Gaussian of fwhm = 1 Å to account for the spatial incoherence.[48]

Ptychography Reconstruction. Ptychography reconstruction was performed using a homemade python script reproducing the MATLAB code used in ref49. This code used the ePIE method[50] to reconstruct the complex incident probe and the corresponding deconvolved object phase.

Density Functional Theory. First-principles calculations are performed based on density functional theory (DFT), norm-conserving pseudopotentials, and pseudoatomic localized basis functions using the GPAW software package.[46] The Perdew–Burke–Ernzerhof[51] implementation of the generalized-gradient approximation functional is used to describe the exchange-correlation interaction. Applying the Monkhorst–Pack scheme,[52] the electronic structure of TMDs are computed with a k-points sampling equivalent to a 12 × 12 × 1 mesh in the unit cell. To avoid spurious interaction, an interlayer distance of 25 Å is employed between the periodically repeated images. The atoms are characterized using a basis set defined from a linear combination of atomic orbitals with two radial functions per valence state and a polarization function, namely, the double-ζ polarized. The computations yield 3.34 Å for the lattice parameters of WSe_2, in good agreement with the literature.[53] Similarly, the estimated band gap of 1.53 eV is in agreement with those from previous DFT calculations.[54] In order to model negatively charged V dopants, an attractive point charge potential (q_{pc} = 0.25e) is located at the defect site, resulting in an accumulation of negative charge of q = −0.45e, as calculated by Bader charge analysis.[55] This method allows to simulate charge localization by avoiding standard delocalization errors related to semilocal functionals in DFT.[56] Further information on the computational framework and its caveats is given in the Supporting Information.

ASSOCIATED CONTENT

Supporting Information

The Supporting Information is available free of charge at https://pubs.acs.org/doi/10.1021/acsnano.4c06561.

HAADF imaging of V-doped WSe_2; structure of 4|4P mirror twin boundary; effect of 3-fold astigmatism on CoM-based reconstruction and HAADF imaging; dopant charge visibility in the reconstructed images of electric field, potential, and charge density; potential around a neutral (noncharged) vanadium dopant; ptychography object phase reconstructions; independent atom model simulation on a defect-rich model; large-scale mapping of electric field and electrostatic potential; first-principles computational framework; modeling charge injection from first-principles for STEM image simulations; effects of defects interaction on the first-principles electronic structure (PDF)

AUTHOR INFORMATION

Corresponding Author

Hanako Okuno − *Univ. Grenoble Alpes, CEA, IRIG-MEM, 38000 Grenoble, France;* orcid.org/0000-0002-7688-9526; Email: hanako.okuno@cea.fr

Authors

Djordje Dosenovic − *Univ. Grenoble Alpes, CEA, IRIG-MEM, 38000 Grenoble, France;* orcid.org/0009-0000-8531-8904

Samuel Dechamps − *Univ. Grenoble Alpes, CEA, IRIG-MEM, 38000 Grenoble, France; Institute of Condensed Matter and Nanosciences, Université catholique de Louvain (UCLouvain), 1348 Louvain-la-Neuve, Belgium*

Kshipra Sharma − *Univ. Grenoble Alpes, CEA, IRIG-MEM, 38000 Grenoble, France*

Jean-Luc Rouviere − *Univ. Grenoble Alpes, CEA, IRIG-MEM, 38000 Grenoble, France*

Yiran Lu − *Univ. Grenoble Alpes, CNRS-Institut Néel, F-38000 Grenoble, France;* orcid.org/0009-0001-7950-9234

Martien Ilse den Hertog − *Univ. Grenoble Alpes, CNRS-Institut Néel, F-38000 Grenoble, France;* orcid.org/0000-0003-0781-9249

Luigi Genovese − *Univ. Grenoble Alpes, CEA, IRIG-MEM, 38000 Grenoble, France;* orcid.org/0000-0003-1747-0247

Simon Mutien-Marie Dubois − *Institute of Condensed Matter and Nanosciences, Université catholique de Louvain (UCLouvain), 1348 Louvain-la-Neuve, Belgium*

Jean-Christophe Charlier − *Institute of Condensed Matter and Nanosciences, Université catholique de Louvain (UCLouvain), 1348 Louvain-la-Neuve, Belgium*

Matthieu Jamet − *Univ. Grenoble Alpes, CEA, CNRS, Grenoble INP, IRIG-SPINTEC, 38000 Grenoble, France;* orcid.org/0000-0002-8247-4677

Alain Marty − *Univ. Grenoble Alpes, CEA, CNRS, Grenoble INP, IRIG-SPINTEC, 38000 Grenoble, France*

Complete contact information is available at: https://pubs.acs.org/10.1021/acsnano.4c06561

Author Contributions

The manuscript was written through contributions of all authors. All authors have given approval to the final version of the manuscript.

Notes

The authors declare no competing financial interest.

An earlier version of this work has been made available on arXiv.[57]

ACKNOWLEDGMENTS

The authors acknowledge the French National Research Agency through the MAGICVALLEY project (ANR-18-CE24-0007). The LANEF framework (No. ANR-10-LABX-0051) is acknowledged for its support with mutualized infrastructure. This project received funding from the European Research Council under the European Union's H2020 Research and Innovation program via the e-See project (Grant No. 758385). S.D., S.M.-M.D., and J.-C.C. acknowledge financial support from the European Union's Horizon 2020 Research Project and Innovation Program—Graphene Flagship Core3 (N° 881603), from the Fédération Wallonie-Bruxelles through the ARC Grant "DREAMS" (N° 21/26-116) and the EOS project

"CONNECT" (N° 40007563), by the Flag-ERA JTC 2019 project entitled "SOGraphMEM" (ANR-19-GRFI-0001-07, R.8012.19), and from the Belgium F.R.S.-FNRS through the research project (N° T.029.22F). Computational resources have been provided by the CISM supercomputing facilities of UCLouvain and the CÉCI consortium funded by F.R.S.-FNRS of Belgium (N° 2.5020.11). These experiments have been performed at the Nanocharacterisation platform in Minatec, Grenoble. The authors acknowledge Dr. Matthew Bryan for his help in ptychography data treatments.

REFERENCES

(1) Novoselov, K. S.; Mishchenko, A.; Carvalho, A.; Castro Neto, A. H. 2D Materials and van Der Waals Heterostructures. *Science* **2016**, *353* (6298), No. aac9439.
(2) Fiori, G.; Bonaccorso, F.; Iannaccone, G.; Palacios, T.; Neumaier, D.; Seabaugh, A.; Banerjee, S. K.; Colombo, L. Electronics Based on Two-Dimensional Materials. *Nat. Nanotechnol.* **2014**, *9* (10), 768−779.
(3) Sierra, J. F.; Fabian, J.; Kawakami, R. K.; Roche, S.; Valenzuela, S. O. Van Der Waals Heterostructures for Spintronics and Opto-Spintronics. *Nat. Nanotechnol.* **2021**, *16* (8), 856−868.
(4) Yang, H.; Valenzuela, S. O.; Chshiev, M.; Couet, S.; Dieny, B.; Dlubak, B.; Fert, A.; Garello, K.; Jamet, M.; Jeong, D.-E.; Lee, K.; Lee, T.; Martin, M.-B.; Kar, G. S.; Sénéor, P.; Shin, H.-J.; Roche, S. Two-Dimensional Materials Prospects for Non-Volatile Spintronic Memories. *Nature* **2022**, *606* (7915), 663−673.
(5) Zhang, L.; Dong, J.; Ding, F. Strategies, Status, and Challenges in Wafer Scale Single Crystalline Two-Dimensional Materials Synthesis. *Chem. Rev.* **2021**, *121* (11), 6321−6372.
(6) Loh, L.; Zhang, Z.; Bosman, M.; Eda, G. Substitutional Doping in 2D Transition Metal Dichalcogenides. *Nano Res.* **2021**, *14* (6), 1668−1681.
(7) Lin, Y.-C.; Torsi, R.; Geohegan, D. B.; Robinson, J. A.; Xiao, K. Controllable Thin-Film Approaches for Doping and Alloying Transition Metal Dichalcogenides Monolayers. *Adv. Sci.* **2021**, *8* (9), No. 2004249.
(8) Cheng, Y. C.; Zhu, Z. Y.; Mi, W. B.; Guo, Z. B.; Schwingenschlögl, U. Prediction of Two-Dimensional Diluted Magnetic Semiconductors: Doped Monolayer MoS2 Systems. *Phys. Rev. B* **2013**, *87* (10), No. 100401.
(9) Mishra, R.; Zhou, W.; Pennycook, S. J.; Pantelides, S. T.; Idrobo, J.-C. Long-Range Ferromagnetic Ordering in Manganese-Doped Two-Dimensional Dichalcogenides. *Phys. Rev. B* **2013**, *88* (14), No. 144409.
(10) Tiwari, S.; Van de Put, M. L.; Sorée, B.; Vandenberghe, W. G. Magnetic Order and Critical Temperature of Substitutionally Doped Transition Metal Dichalcogenide Monolayers. *npj 2D Mater. Appl.* **2021**, *5* (1), 54.
(11) Duong, D. L.; Yun, S. J.; Kim, Y.; Kim, S.-G.; Lee, Y. H. Long-Range Ferromagnetic Ordering in Vanadium-Doped WSe2 Semiconductor. *Appl. Phys. Lett.* **2019**, *115* (24), No. 242406.
(12) Yun, S. J.; Duong, D. L.; Ha, D. M.; Singh, K.; Phan, T. L.; Choi, W.; Kim, Y.-M.; Lee, Y. H. Ferromagnetic Order at Room Temperature in Monolayer WSe2 Semiconductor via Vanadium Dopant. *Adv. Sci.* **2020**, *7* (9), No. 1903076.
(13) Lin, X.; Ni, J. Charge and Magnetic States of Mn-, Fe-, and Co-Doped Monolayer MoS2. *J. Appl. Phys.* **2014**, *116* (4), No. 044311.
(14) Robertson, A. W.; Lin, Y.-C.; Wang, S.; Sawada, H.; Allen, C. S.; Chen, Q.; Lee, S.; Lee, G.-D.; Lee, J.; Han, S.; Yoon, E.; Kirkland, A. I.; Kim, H.; Suenaga, K.; Warner, J. H. Atomic Structure and Spectroscopy of Single Metal (Cr, V) Substitutional Dopants in Monolayer MoS2. *ACS Nano* **2016**, *10* (11), 10227−10236.
(15) Barja, S.; Refaely-Abramson, S.; Schuler, B.; Qiu, D. Y.; Pulkin, A.; Wickenburg, S.; Ryu, H.; Ugeda, M. M.; Kastl, C.; Chen, C.; Hwang, C.; Schwartzberg, A.; Aloni, S.; Mo, S.-K.; Ogletree, D. F.; Crommie, M. F.; Yazyev, O. V.; Louie, S. G.; Neaton, J. B.; Weber-Bargioni, A. Identifying Substitutional Oxygen as a Prolific Point Defect in Monolayer Transition Metal Dichalcogenides. *Nat. Commun.* **2019**, *10* (1), No. 3382.
(16) Shibata, N.; Findlay, S. D.; Kohno, Y.; Sawada, H.; Kondo, Y.; Ikuhara, Y. Differential Phase-Contrast Microscopy at Atomic Resolution. *Nat. Phys.* **2012**, *8* (8), 611−615.
(17) Ophus, C. Four-Dimensional Scanning Transmission Electron Microscopy (4D-STEM): From Scanning Nanodiffraction to Ptychography and Beyond. *Microsc. Microanal.* **2019**, *25* (3), 563−582.
(18) Ehrenfest, P. Bemerkung über die angenäherte Gültigkeit der klassischen Mechanik innerhalb der Quantenmechanik. *Z. Phys.* **1927**, *45* (7), 455−457.
(19) Müller, K.; Krause, F. F.; Béché, A.; Schowalter, M.; Galioit, V.; Löffler, S.; Verbeeck, J.; Zweck, J.; Schattschneider, P.; Rosenauer, A. Atomic Electric Fields Revealed by a Quantum Mechanical Approach to Electron Picodiffraction. *Nat. Commun.* **2014**, *5* (1), No. 5653.
(20) Chen, Z.; Jiang, Y.; Shao, Y.-T.; Holtz, M. E.; Odstrčil, M.; Guizar-Sicairos, M.; Hanke, I.; Ganschow, S.; Schlom, D. G.; Muller, D. A. Electron Ptychography Achieves Atomic-Resolution Limits Set by Lattice Vibrations. *Science* **2021**, *372* (6544), 826−831.
(21) Calderon V, S.; Ferreira, R. V.; Taneja, D.; Jayanth, R.; Zhou, L.; Ribeiro, R. M.; Akinwande, D.; Ferreira, P. J. Atomic Electrostatic Maps of Point Defects in MoS2. *Nano Lett.* **2021**, *21* (24), 10157−10164.
(22) Fang, S.; Wen, Y.; Allen, C. S.; Ophus, C.; Han, G. G. D.; Kirkland, A. I.; Kaxiras, E.; Warner, J. H. Atomic Electrostatic Maps of 1D Channels in 2D Semiconductors Using 4D Scanning Transmission Electron Microscopy. *Nat. Commun.* **2019**, *10* (1), No. 1127.
(23) Wen, Y.; Fang, S.; Coupin, M.; Lu, Y.; Ophus, C.; Kaxiras, E.; Warner, J. H. Mapping 1D Confined Electromagnetic Edge States in 2D Monolayer Semiconducting MoS2 Using 4D-STEM. *ACS Nano* **2022**, *16* (4), 6657−6665.
(24) Ishikawa, R.; Findlay, S. D.; Seki, T.; Sánchez-Santolino, G.; Kohno, Y.; Ikuhara, Y.; Shibata, N. Direct Electric Field Imaging of Graphene Defects. *Nat. Commun.* **2018**, *9* (1), No. 3878.
(25) Müller-Caspary, K.; Duchamp, M.; Rösner, M.; Migunov, V.; Winkler, F.; Yang, H.; Huth, M.; Ritz, R.; Simson, M.; Ihle, S.; Soltau, H.; Wehling, T.; Dunin-Borkowski, R. E.; Van Aert, S.; Rosenauer, A. Atomic-Scale Quantification of Charge Densities in Two-Dimensional Materials. *Phys. Rev. B* **2018**, *98* (12), No. 121408.
(26) Martis, J.; Susarla, S.; Rayabharam, A.; Su, C.; Paule, T.; Pelz, P.; Huff, C.; Xu, X.; Li, H.-K.; Jaikissoon, M.; Chen, V.; Pop, E.; Saraswat, K.; Zettl, A.; Aluru, N. R.; Ramesh, R.; Ercius, P.; Majumdar, A. Imaging the Electron Charge Density in Monolayer MoS2 at the Ångstrom Scale. *Nat. Commun.* **2023**, *14* (1), No. 4363.
(27) Susana, L.; Gloter, A.; Tencé, M.; Zobelli, A. Direct Quantifying Charge Transfer by 4D-STEM: A Study on Perfect and Defective Hexagonal Boron Nitride. *ACS Nano* **2024**, *18* (10), 7424−7432.
(28) Mallet, P.; Chiapello, F.; Okuno, H.; Boukari, H.; Jamet, M.; Veuillen, J.-Y. Bound Hole States Associated to Individual Vanadium Atoms Incorporated into Monolayer ${\mathrm{WSe}}_{2}$. *Phys. Rev. Lett.* **2020**, *125* (3), No. 036802.
(29) Wang, Y.; Zheng, Y.; Xu, X.; Dubuisson, E.; Bao, Q.; Lu, J.; Loh, K. P. Electrochemical Delamination of CVD-Grown Graphene Film: Toward the Recyclable Use of Copper Catalyst. *ACS Nano* **2011**, *5* (12), 9927−9933.
(30) Komsa, H.-P.; Kotakoski, J.; Kurasch, S.; Lehtinen, O.; Kaiser, U.; Krasheninnikov, A. V. Two-Dimensional Transition Metal Dichalcogenides under Electron Irradiation: Defect Production and Doping. *Phys. Rev. Lett.* **2012**, *109* (3), No. 035503.
(31) Savitzky, B. H.; Zeltmann, S. E.; Hughes, L. A.; Brown, H. G.; Zhao, S.; Pelz, P. M.; Pekin, T. C.; Barnard, E. S.; Donohue, J.; DaCosta, L. R.; Kennedy, E.; Xie, Y.; Janish, M. T.; Schneider, M. M.; Herring, P.; Gopal, C.; Anapolsky, A.; Dhall, R.; Bustillo, K. C.; Ercius, P.; Scott, M. C.; Ciston, J.; Minor, A. M.; Ophus, C. py4DSTEM: A Software Package for Four-Dimensional Scanning Transmission Electron Microscopy Data Analysis. *Microsc. Microanal.* **2021**, *27* (4), 712−743.
(32) Kozhakhmetov, A.; Stolz, S.; Tan, A. M. Z.; Pendurthi, R.; Bachu, S.; Turker, F.; Alem, N.; Kachian, J.; Das, S.; Hennig, R. G.; Gröning, O.; Schuler, B.; Robinson, J. A. Controllable P-Type Doping of 2D WSe2 via Vanadium Substitution. *Adv. Funct. Mater.* **2021**, *31* (42), No. 2105252.

https://doi.org/10.1021/acsnano.4c06561
ACS Nano 2024, 18, 23354−23364

(33) Komsa, H.-P.; Krasheninnikov, A. V. Engineering the Electronic Properties of Two-Dimensional Transition Metal Dichalcogenides by Introducing Mirror Twin Boundaries. *Adv. Electron. Mater.* **2017**, *3* (6), No. 1600468.
(34) Pathirage, V.; Lasek, K.; Krasheninnikov, A. V.; Komsa, H. P.; Batzill, M. Mirror Twin Boundaries in WSe2 Induced by Vanadium Doping. *Mater. Today Nano* **2023**, *22*, No. 100314.
(35) Lehtinen, O.; Komsa, H.-P.; Pulkin, A.; Whitwick, M. B.; Chen, M.-W.; Lehnert, T.; Mohn, M. J.; Yazyev, O. V.; Kis, A.; Kaiser, U.; Krasheninnikov, A. V. Atomic Scale Microstructure and Properties of Se-Deficient Two-Dimensional MoSe2. *ACS Nano* **2015**, *9* (3), 3274−3283.
(36) Hong, J.; Wang, C.; Liu, H.; Ren, X.; Chen, J.; Wang, G.; Jia, J.; Xie, M.; Jin, C.; Ji, W.; Yuan, J.; Zhang, Z. Inversion Domain Boundary Induced Stacking and Bandstructure Diversity in Bilayer MoSe2. *Nano Lett.* **2017**, *17* (11), 6653−6660.
(37) Lopatin, S.; Aljarb, A.; Roddatis, V.; Meyer, T.; Wan, Y.; Fu, J.-H.; Hedhili, M.; Han, Y.; Li, L.-J.; Tung, V. Aberration-Corrected STEM Imaging of 2D Materials: Artifacts and Practical Applications of Threefold Astigmatism. *Sci. Adv.* **2020**, *6* (37), No. eabb8431.
(38) Hofer, C.; Skákalová, V.; Haas, J.; Wang, X.; Braun, K.; Pennington, R. S.; Meyer, J. C. Atom-by-Atom Chemical Identification from Scanning Transmission Electron Microscopy Images in Presence of Noise and Residual Aberrations. *Ultramicroscopy* **2021**, *227*, No. 113292.
(39) Dosenovic, D.; Dechamps, S.; Vergnaud, C.; Pasko, S.; Krotkus, S.; Heuken, M.; Genovese, L.; Rouviere, J.-L.; den Hertog, M.; Van-Jodin, L. L.; Jamet, M.; Marty, A.; Okuno, H. Mapping Domain Junctions Using 4D-STEM: Toward Controlled Properties of Epitaxially Grown Transition Metal Dichalcogenide Monolayers. *2D Mater.* **2023**, *10* (4), No. 045024.
(40) Wen, Y.; Ophus, C.; Allen, C. S.; Fang, S.; Chen, J.; Kaxiras, E.; Kirkland, A. I.; Warner, J. H. Simultaneous Identification of Low and High Atomic Number Atoms in Monolayer 2D Materials Using 4D Scanning Transmission Electron Microscopy. *Nano Lett.* **2019**, *19* (9), 6482−6491.
(41) Stolz, S.; Kozhakhmetov, A.; Dong, C.; Gröning, O.; Robinson, J. A.; Schuler, B. Layer-Dependent Schottky Contact at van Der Waals Interfaces: V-Doped WSe2 on Graphene. *npj 2D Mater. Appl.* **2022**, *6* (1), 66.
(42) Egerton, R. F.; Li, P.; Malac, M. Radiation Damage in the TEM and SEM. *Micron* **2004**, *35* (6), 399−409.
(43) McDonnell, S.; Addou, R.; Buie, C.; Wallace, R. M.; Hinkle, C. L. Defect-Dominated Doping and Contact Resistance in MoS2. *ACS Nano* **2014**, *8* (3), 2880−2888.
(44) Hus, S. M.; Li, A.-P. Spatially-Resolved Studies on the Role of Defects and Boundaries in Electronic Behavior of 2D Materials. *Prog. Surf. Sci.* **2017**, *92* (3), 176−201.
(45) Madsen, J.; Susi, T. The abTEM Code: Transmission Electron Microscopy from First Principles. *Open Res. Eur.* **2021**, *1*, 24.
(46) Mortensen, J. J.; Hansen, L. B.; Jacobsen, K. W. Real-Space Grid Implementation of the Projector Augmented Wave Method. *Phys. Rev. B* **2005**, *71* (3), No. 035109.
(47) Lobato, I.; Van Dyck, D. An Accurate Parameterization for Scattering Factors, Electron Densities and Electrostatic Potentials for Neutral Atoms That Obey All Physical Constraints. *Acta Crystallogr., Sect. A: Found. Adv.* **2014**, *70* (6), 636−649.
(48) Oxley, M. P.; Dyck, O. E. The Importance of Temporal and Spatial Incoherence in Quantitative Interpretation of 4D-STEM. *Ultramicroscopy* **2020**, *215*, No. 113015.
(49) Jiang, Y.; Chen, Z.; Han, Y.; Deb, P.; Gao, H.; Xie, S.; Purohit, P.; Tate, M. W.; Park, J.; Gruner, S. M.; Elser, V.; Muller, D. A. Electron Ptychography of 2D Materials to Deep Sub-Ångström Resolution. *Nature* **2018**, *559* (7714), 343−349.
(50) Maiden, A. M.; Rodenburg, J. M. An Improved Ptychographical Phase Retrieval Algorithm for Diffractive Imaging. *Ultramicroscopy* **2009**, *109* (10), 1256−1262.
(51) Perdew, J. P.; Yue, W. Accurate and Simple Density Functional for the Electronic Exchange Energy: Generalized Gradient Approximation. *Phys. Rev. B* **1986**, *33* (12), 8800−8802.
(52) Monkhorst, H. J.; Pack, J. D. Special Points for Brillouin-Zone Integrations. *Phys. Rev. B* **1976**, *13* (12), 5188−5192.
(53) Schutte, W. J.; De Boer, J. L.; Jellinek, F. Crystal Structures of Tungsten Disulfide and Diselenide. *J. Solid State Chem.* **1987**, *70* (2), 207−209.
(54) Zhang, C.; Gong, C.; Nie, Y.; Min, K.-A.; Liang, C.; Oh, Y. J.; Zhang, H.; Wang, W.; Hong, S.; Colombo, L.; Wallace, R. M.; Cho, K. Systematic Study of Electronic Structure and Band Alignment of Monolayer Transition Metal Dichalcogenides in Van Der Waals Heterostructures. *2D Mater.* **2017**, *4* (1), No. 015026.
(55) Henkelman, G.; Arnaldsson, A.; Jónsson, H. A Fast and Robust Algorithm for Bader Decomposition of Charge Density. *Comput. Mater. Sci.* **2006**, *36* (3), 354−360.
(56) Cohen, A. J.; Mori-Sánchez, P.; Yang, W. Insights into Current Limitations of Density Functional Theory. *Science* **2008**, *321* (5890), 792−794.
(57) Dosenovic, D.; Sharma, K.; Dechamps, S.; Rouviere, J.-L.; Lu, Y.; Mordant, A.; den Hertog, M.; Genovese, L.; Dubois, S. M.-M.; Charlier, J.-C.; Jamet, M.; Marty, A.; Okuno, H. Atomic Scale Imaging of the Negative Charge Induced by a Single Vanadium Dopant Atom in Monolayer WSe_2 Using 4D-STEM. 2023, arxiv:2310.09246. arXiv.org e-Print archive. https://arxiv.org/abs/2310.09246 (accessed July 28, 2024).

https://doi.org/10.1021/acsnano.4c06561
ACS Nano 2024, 18, 23354−23364